

# A mesoscale self-assembly into bulk bassanite via delicate control of water activity to mimic biomineralization

**Chunli Wang**

University of Chinese Academy of Sciences

**Xuelu Ma**

maxl@cumtb.edu.cn

**Zhihao Zhang**

1206777500@qq.com

**Hai Xiao**

Tsinghua University

**Xianlai Zeng**

Tsinghua University

**Jing Zhang** (✉ [jingzhang@ucas.ac.cn](mailto:jingzhang@ucas.ac.cn))

University of Chinese Academy of Sciences

**Zhang Lin**

Central South University

---

## Article

### Keywords:

**Posted Date:** April 5th, 2022

**DOI:** <https://doi.org/10.21203/rs.3.rs-1508202/v1>

**License:** © ⓘ This work is licensed under a Creative Commons Attribution 4.0 International License.

[Read Full License](#)

---

# A mesoscale self-assembly into bulk bassanite via delicate control of water activity to mimic biomineralization

Chunli Wang <sup>a, b</sup>, Xuelu Ma <sup>c</sup>, Zhihao Zhang <sup>a</sup>, Hai Xiao <sup>d</sup>, Xianlai Zeng <sup>e</sup>, Jing Zhang <sup>a, b, \*</sup>, Zhang Lin <sup>a,</sup>

<sup>b, \*</sup>

<sup>a</sup>*Research Center for Environmental Material and Pollution Control Technology, University of Chinese Academy of Sciences, Beijing 101408, China*

<sup>b</sup>*Chinese National Engineering Research Centre for Control & Treatment of Heavy Metal Pollution, School of Metallurgy and Environment, Central South University, Changsha 410083, China.*

<sup>c</sup>*School of Chemistry and Environmental Engineering, China University of Mining and Technology-Beijing, Beijing 100085, China*

<sup>d</sup>*Department of Chemistry, Tsinghua University, Beijing 100084, China.*

<sup>e</sup>*State Key Joint Laboratory of Environment Simulation and Pollution Control, School of Environment, Tsinghua University, Beijing 100084, China.*

\* Corresponding authors: jingzhang@rcees.ac.cn (J. Z.); zhang\_lin@csu.edu.cn (Z. L.)

Metastable bassanite cannot usually be precipitated from aqueous solutions, yet easily taking up water to yield the gypsum. Although biological systems can mineralize this phase to micron sized crystals, a facile fabrication of bulk bassanite in vitro under ambient conditions remains a major challenge. Here, we unprecedentedly fabricated the bulk phase of bassanite by precisely controlling the water limited in the solution with polymer (polyvinyl pyrrolidone), suppressing the transformation into thermodynamically favourable gypsum. A new thermodynamic model of the non-classical crystallization process is described in terms of water-driven colloidal assembly, and molecular dynamics simulation demonstrates the role of water molecules to interact with the polymer ligands to initiate the assembly and growth of bassanite. These findings contribute to a deeper understanding of how the bassanite precipitates in vivo and may save us the procedure of thermally transforming about hundreds of millions of tons of dihydrate per year into hemihydrate.

## Introduction

Calcium sulfate minerals are widespread throughout the Earth, where gypsum ( $\text{CaSO}_4 \cdot 2\text{H}_2\text{O}$ ) and anhydrite ( $\text{CaSO}_4$ ) can naturally deposit on terrestrial surfaces<sup>1,2</sup>, while bassanite ( $\text{CaSO}_4 \cdot 0.5\text{H}_2\text{O}$ ) is unstable and transient, and thus only occurs in small quantities near the land surface in arid regions<sup>3,4</sup>. Recently, bassanite is massively found on Mars<sup>5,6</sup>, yet why the thermodynamically unstable bassanite phase persists on Mars is still debated. In industry, about 100 billion bassanite was produced by an energy intensive dehydration of gypsum per year around the world<sup>7,8</sup>. Alternatively, natural organisms provide an energy-saving way to produce stable bulk bassanite. For example, micron sized bassanite was found in statoliths of deep-sea medusae for gravity sensing<sup>9</sup>, although the sea-living organisms are consisting mostly of water<sup>10</sup>. Similar bassanite is also found in the wood of the Tamarix tree<sup>11</sup>. However, the fabrication of bulk bassanite in vitro is by no means a low hanging fruit, due to its easy hydration and thermodynamic instability<sup>3</sup>.

The crystallization of mesoscale bulk biomimetic materials is a frequently occurring via the mechanism of particle assembly<sup>12,13</sup>, in which primary particles align along specific crystallographic directions to attach and coalesce into a bigger one<sup>14</sup>. In the assembly process, metastable precursor particles often spontaneously transform into the thermodynamically favoured phase at a bulk size. A transient conversion from metastable bassanite nanoparticles into micrometre-sized gypsum crystals was observed to experience the oriented attachment dominating growth process<sup>3</sup>. The phase transformation of bassanite undergoes a very fast coarsening process even at the very early stage of nanoparticles<sup>15</sup>. In this scenario, water can not only accelerate nanocrystal growth, but also trigger phase transformation into gypsum at the same time. This explains why bassanite minerals are rarely found in the natural aqueous environment. When water is not precisely controlled during the crystallization of the above water-sensitive systems, either nanosized metastable bassanite or bulk gypsum phase can be obtained in solution, but hardly achieving stable bulk bassanite at ambient conditions<sup>16</sup>. Fortunately, the evidences of bassanite present on Mars and in some living organisms provide a clue that water activity in the surroundings might play a critical role in determining the fate of calcium sulfate phases during crystallization<sup>17,18</sup>.

Considering that the nucleation and growth of bassanite is extremely sensitive to the surrounding water that can be mediated by bio-macromolecules<sup>19</sup>, we propose a two-steps strategy to limit water activity by polymers, with the aim to control the water-involved crystal growth and phase transformation process of calcium sulfate. By limiting water in the n-propanol (NPA) solution with polyvinyl pyrrolidone (PVP), the water available for phase transformation of bassanite is under well controlled. In this way, the water-driven hierarchical assembly of calcium sulfate nanorod precursors into mesoscale structures can be realized to form final bassanite phase at the bulk size, without transforming into gypsum. To the best of our knowledge, the bassanite of meso/bulk crystal obtained in solution at room temperature has yet been reported in the literatures. Based on the experimental observation, thermodynamic modelling and *Ab initio* molecular dynamics (AIMD) were performed to understand the effect of organic ligands on water-induced aggregation and crystallization of bassanite. Our work not only proposed a strategy to produce stable bulk bassanite beyond traditional dehydration upon heat-treatment for energy-efficient application, but also helps to understand how the metastable bassanite can persist in the regions of low water activity on Mars or in other severe arid conditions, as a potential water source for organismal survival.

## **Results**

### **Formation of bulk bassanite.**

Deep-sea medusae (Fig. 1A), a sea-living organisms consisting mostly of water, use water-deficient bassanite for gravity sensing (Fig. 1B)<sup>9</sup>. This biological system actively induces the crystallisation of this phase far away from chemical equilibrium. Herein a two-step strategy of mimicry is designed to precisely control the evolution of calcium sulfate phases in solution at room temperature (Supplementary Fig. 1).

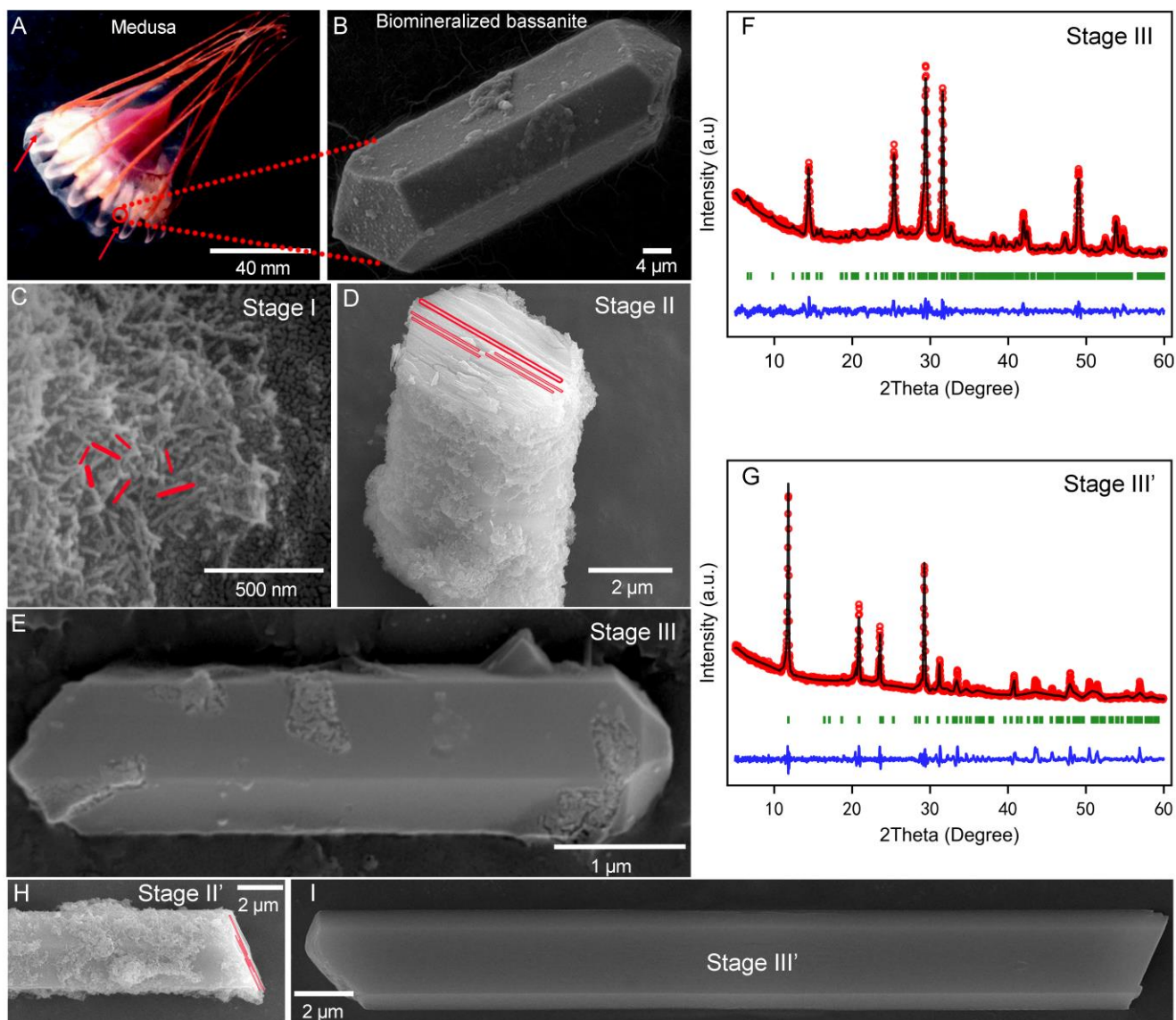


**Fig. 1 Evolution of bassanite.** (A) Bassanite formed in deep-sea medusae. (B) The medusa *Periphylla periphylla* with positions of bassanite indicated (arrows) (9). (C) Precursor of bassanite nanorods formed in Stage I. The red rectangle outlines the out-of-order stacking of bassanite nanorods. (D) Mesostructured bassanite assembled by nanorod precursor collected at 10 min (Stage II) after adding 3.85 wt% of water in (C), the red lines emphasize the bassanite nanorod units. (E) Bulk bassanite with a prismatic shape and clear facets at 30 min (Stage II). (F, G) XRD patterns showing bassanite (F) and gypsum (G) formed at Stage III and Stage III', respectively. (H, I) Mesostructured and bulk gypsum formed at 10 min (Stage II') (H) and 30 min (Stage III') (I), respectively, after adding 19.35 wt% water in (C).

In the first step, the calcium sulfate colloids are prepared in the NPA solution by employing PVP as the surface-bound ligands (Stage I). The as-obtained calcium sulfate precursor has a bassanite structure with a gyration radius of about 45 nm (Supplementary Fig. 2), and emerges as the randomly orientated nanorods with a diameter of about 20 nm and a length of about 200 nm (Fig. 1C). In the following step, water is precisely added into the suspensions of bassanite precursors formed in Stage I. When 3.85 wt%

of water (molar ratio of  $\text{H}_2\text{O}/\text{CaSO}_4 = 22.25$ ) was introduced, the rod-shaped aggregate appears after 10 min of reaction (Stage II) (Fig. 1D). In the mesostructure, bassanite nanorod precursors originally formed in Stage I are still clearly visible and act as the building units to laterally orientate and organize into the mesostructured assembly<sup>20</sup>. 30 minutes later, the mesostructure continuously grow and finally form the bulk (Stage III) (Fig. 1E), which is morphologically very similar to the bassanite (Fig. 1B) formed in deep-sea medusae (Fig. 1F). Impressively, it shows a prismatic shape of clear facets, with a length of about 5.03  $\mu\text{m}$  and a transverse size of about 1.28  $\mu\text{m}$ . Moreover, the bulk phase presents a clean bassanite structure, as identified by XRD (Fig. 1F) and infrared spectra (IR) (Supplementary Fig. 3), and the product keeps stable afterwards even after 24 hours (Supplementary Fig. 4). As a control, when a tiny amount of water (1 wt%) is added into the bassanite precursors without PVP, immediately triggers the phase transition of bassanite into bulk gypsum (Supplementary Fig. 5).

The evolution of microscopic structure of bassanite was further observed by high-resolution transmission electron microscopy (HRTEM). As shown in Fig. 2A, the initially formed bassanite nanorod in Stage I is built up by the nanoparticles with a size about 10 nm serving as the “building blocks”. Judging from their crystal lattices with a distance of 0.28 nm, the small nanoparticles prefer to expose the (204) plane, and then to orient and assemble along the [102] direction, followed by attaching to each other to form bassanite nanorods (Refer to Mode 1 in Fig. 2). Alternatively, two small “building blocks” can collide and coalesce together in the direction perpendicular to [102] (Refer to Mode 2), with a clearly observed twin boundary defect inside (Fig. 2B). The assembly of bassanite nanoparticles in the concurrent way of Mode 1 and Mode 2 will lead to the formation of bassanite nanorods with an increasing size in both the radius (20-100 nm) and the length (100-500 nm) (Fig. 1A). In what follows, these bassanite nanorods stand side-by-side to assemble into a secondary aggregate (Fig. 2C and d), and continuously construct the hierarchical mesostructure (Fig. 1D), which subsequently grow into the equilibrium shape of the bulk bassanite crystals (Fig. 1E). It is clearly seen that the growth of bassanite undergoes a two-step particle assembly, where the introduced water could act as the surface-bound agent to promote interfacial reactions between adjacent particles for hierarchical assembly<sup>22,23</sup>. The whole growth process of bassanite via hierarchical assembly is summarized and depicted in Fig. 2E.

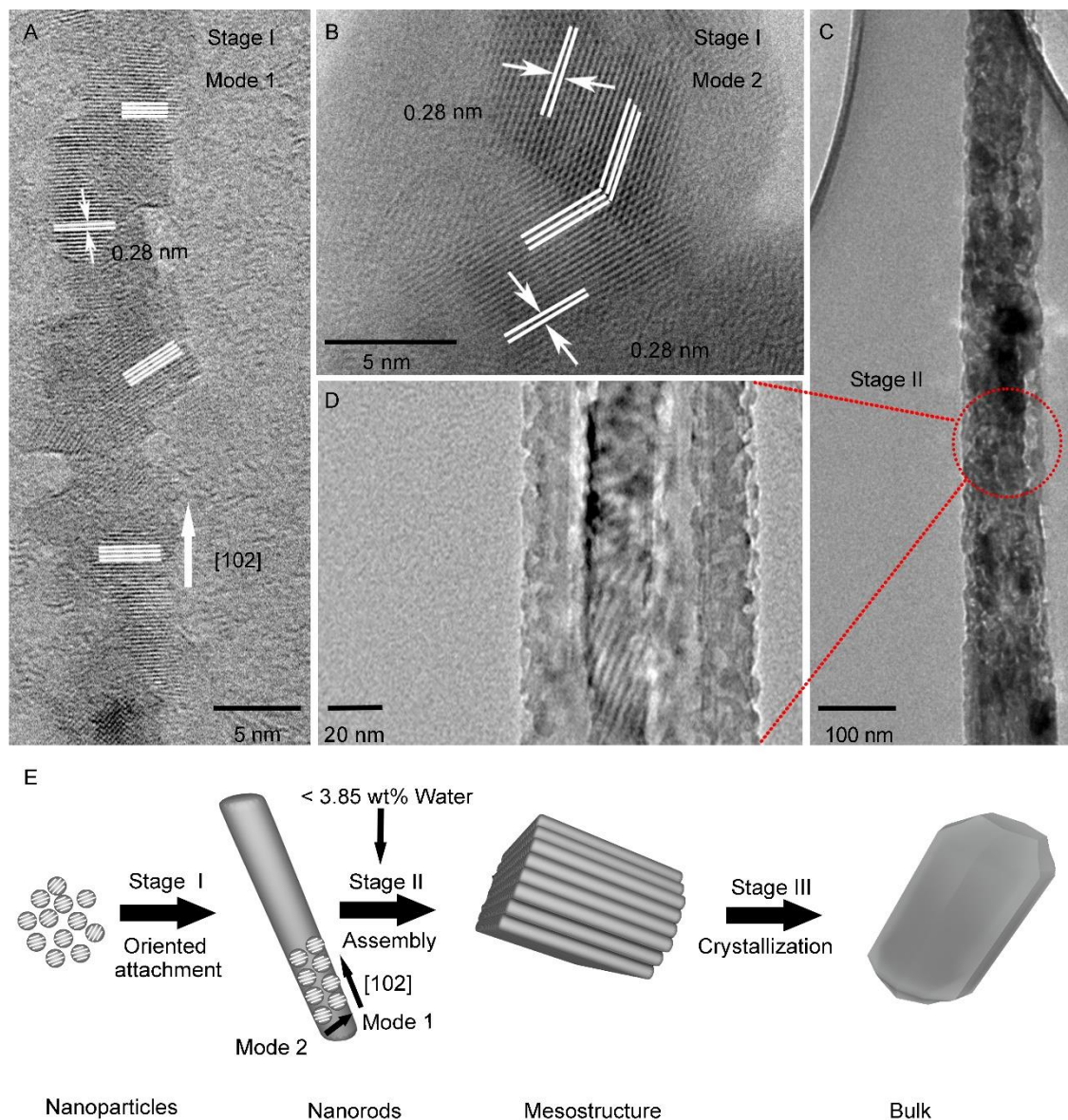


**Fig. 2 Evolution of microscopic structure of bassanite with PVP.** (A, B) HRTEM images of the bassanite nanorods formed in Stage I by assembly of small bassanite nanoparticles in different modes. Mode 1: along the main axis of [102] (A), and Mode 2: in the direction perpendicular to [102] (B). (C, D) HRTEM images of bassanite mesostructure assembling by nanorods with the addition of 3.85 wt% water in Stage II. The magnified area (D) of the mesostructured in (C) clearly shows the assembly and coalescence of bassanite nanorods aligning in their transverse direction. (E) Schematic growth process of bassanite from nanoparticles into bulk.

Further, we simulated the equilibrium shape basing on the surface energy calculated by using density functional theory (DFT) (Supplementary Fig. 6)<sup>24</sup>. The (201) and (111) planes constitute of the main exposed surfaces of the hexagonal bassanite prism, while the (020), (100) and (001) planes construct to the high energy facets (Supplementary Fig. 7-8). This simulation about the Wulff shape of bassanite with the exposed facets agrees well with the experiment results.

However, Further increasing the water ratio more than 3.85% will lead to the occurrence of gypsum, even in the system with PVP (Supplementary Fig. 4). Finally, the nano-bassanite precursor are completely transformed into pure bulk gypsum after adding 13.95 wt% of water at 30 min (see XRD in Fig. 1G and IR in Supplementary Fig. 3), although a similar evolution process from the assembly of primary nanorods into a mesostructure to the final bulk gypsum is also observed (Fig. 1H and 1I)<sup>21</sup>.

### Thermodynamic model.

Based on the above observation, the crystallization of calcium sulphate via hierarchical assembly into bulk phases can be divided in three distinct parts: nucleation, hierarchical assembly and phase transition. Therefore, the change in total Gibbs free energy determining the final products/phases via the aforementioned growth process is associated with three components: (i) formation of BPs ( $\Delta G_{bp}$ ), (ii) assembly of the  $n$  BPs into rod-like assembly ( $\Delta G_{ass-1}$ ), and (iii) further assembly of  $x$  nanorods (building up by BPs) into the secondary rod-shaped aggregates, either still keeping bassanite phase ( $\Delta G_{ass-2}$ ) when adding a small amount of water (e.g. < 3.85 wt%), or converting into gypsum phase ( $\Delta G_{gyp}$ ) at the higher water ratios (see the scheme in Supplementary Fig. 9). For the former case to form bassanite aggregates, the total Gibbs free energy ( $\Delta G_{agg}$ ) can be expressed as:

$$\Delta G_{agg} = nx\Delta G_{bp} + x\Delta G_{ass-1} + \Delta G_{ass-2} \#(1)$$

While for the latter case to transform into gypsum, the total Gibbs free energy ( $\Delta G_{tgy}$ ) is:

$$\Delta G_{tgy} = nx\Delta G_{bp} + x\Delta G_{ass-1} + \Delta G_{gyp} \#(2)$$

The energy difference ( $\Delta G_{dif}$ ) between  $\Delta G_{tgy}$  and  $\Delta G_{agg}$  determines the prior pathway for formation of bassanite assembly ( $\Delta G_{dif} > 0$ ) or conversion into gypsum ( $\Delta G_{dif} < 0$ ), thermodynamically. As the formation of bassanite nanoparticles and nanorods are in the same conditions in Stage I before adding extra water,  $\Delta G_{dif}$  is thus obtained as:

$$\Delta G_{dif} = \Delta G_{tgy} - \Delta G_{agg} = \Delta G_{gyp} - \Delta G_{ass-2} \#(3)$$

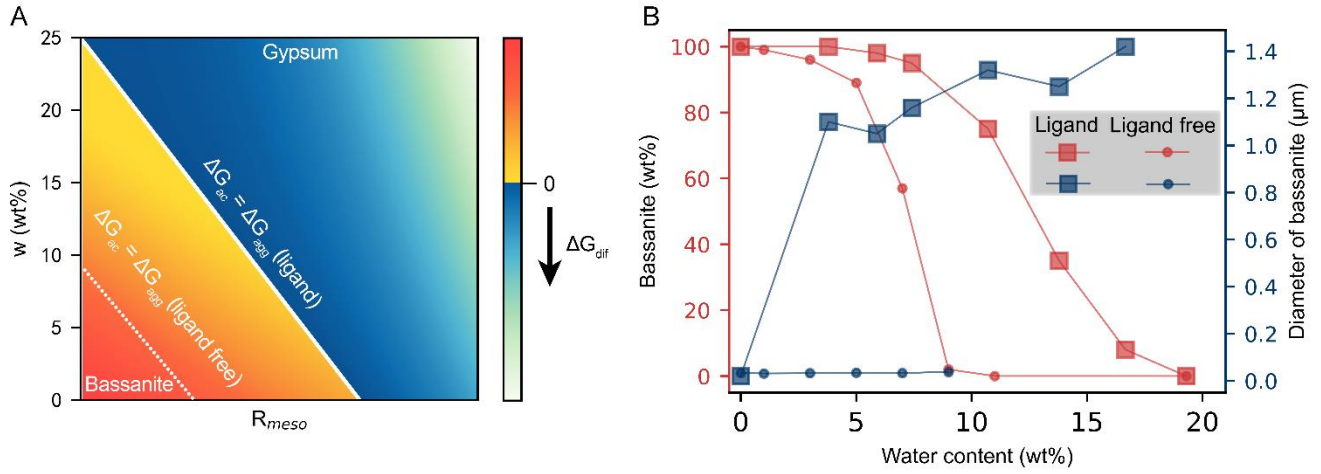


**Fig. 3. Thermodynamic model.** (A) Phase diagram calculated based on the thermodynamic model showing  $\Delta G_{dif}$  as a function of  $w$  and  $R_{meso}$  to favour the formation of either bassanite or gypsum mesocrystals. The white lines indicate the boundary of the two phases at  $\Delta G_{tgy} = \Delta G_{agg}$  in the systems with (solid line) and without (dash line) ligands. Data are generated setting  $\Delta g_{conv} = -0.1 \times 10^6 \text{ kJ}\cdot\text{m}^{-3}$ ,  $\Delta \gamma_{conv} = 2.5 \text{ J}\cdot\text{m}^{-2}$  ( $1 \text{ J}\cdot\text{m}^{-2}$  for the ligand-free system), and  $\Delta \delta_{conv} = -0.1 \text{ J}\cdot\text{m}^{-2}$  ( $-0.11 \text{ J}\cdot\text{m}^{-2}$  for the ligand-free system), as estimates for the generic bulk and surface energy densities of inorganic materials<sup>25</sup>. (B) Experimentally statistical content and average diameter of bassanite obtained by adding different amounts of water into the colloidal bassanite nanorods with or without PVP ligands after staying for 30 min.

The Gibbs free energies ( $\Delta G_{gyp}$  and  $\Delta G_{ass-2}$ ) can write as a function of bulk and surface terms, where the assembly of bassanite particles into the mesostructure is normally assumed not to involve a change in the bulk energy, but just a reduction of the surface term due to a decrease in the interfacial area<sup>26</sup>. Considering the extra water to influence the interfacial energy of PNs, we define the  $\gamma_{meso}$  to describe the new surface Gibbs energy of the secondary rod-shaped bassanite aggregates, and  $\gamma_{meso} = \gamma_{bp} + w\delta_{meso}$ . Here,  $\gamma_{bp}$  is the surface energy for bassanite nanoparticles,  $\delta_{meso}$  represents the surface Gibbs energy variation that can be brought by adding of one percent water (wt%) into the ligands-stabilized bassanite colloid, and  $w$  is the percentage of the water added (wt%). In our case,  $\delta_{meso}$  is positive so that adding more water will induce larger  $\gamma_{meso}$ , which is favourable for assembly of bassanite particles into the mesostructure. Similarly, during the conversion of bassanite into gypsum driven by water, the interfacial energy of gypsum is defined as  $\gamma_{gyp} = \gamma_{gn} + w\delta_{gyp}$ , where  $\delta_{gyp}$ , which is analogue to  $\delta_{meso}$ , represents the surface energy variation changed into gypsum by adding one percent of water and  $\gamma_{gn}$  is the surface energy for gypsum nanoparticles in the absence of the extra water. Therefore, the final expression for  $\Delta G_{dif}$  is obtained as (see more details in Supporting Information):

$$\Delta G_{dif} = 2\pi R_{meso}^2 [4R_{meso}\Delta g_{conv} + 9w\Delta\delta_{conv} + 9\Delta\gamma_{conv}] \#(4)$$

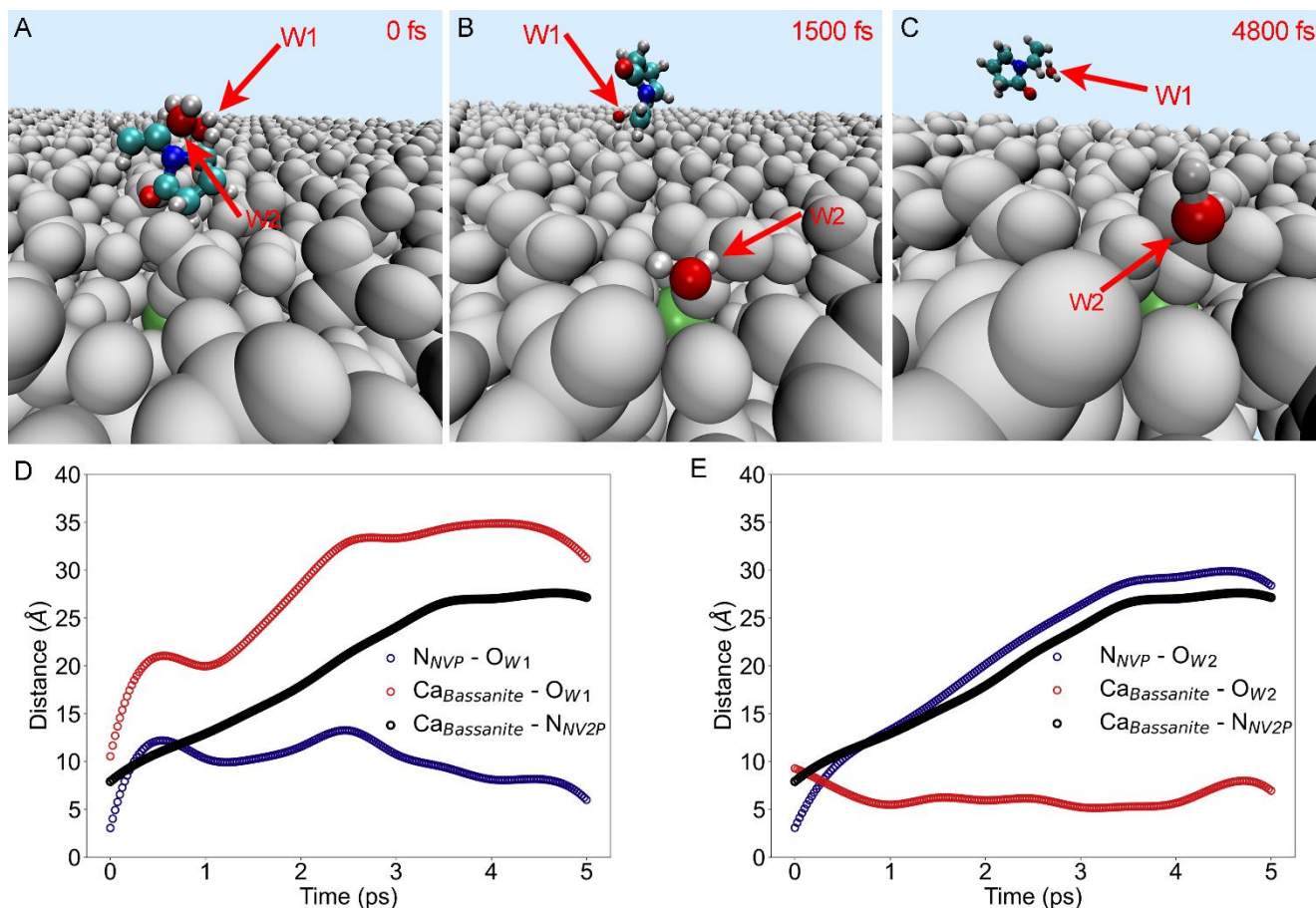
where  $\Delta g_{conv} = g_{gyp} - g_{bp}$ ,  $\Delta\delta_{conv} = \delta_{gyp} - \delta_{meso}$  and  $\Delta\gamma_{conv} = \gamma_{gn} - \gamma_{bp}$ .  $R_{meso}$  is the radius of the corresponding mesocrystal aggregates of either bassanite or converted gypsum (Stage II).  $g_{gyp}$  and  $g_{bp}$  represent bulk energy densities of gypsum and bassanite, respectively. The value of water-dependent  $\Delta\delta_{conv}$  can be estimated according to its effect on the phase conversion boundary, as discussed in-detail in Supplementary Fig. 10.

Fig. 3A illustrates the estimated phase diagram of the formation of bassanite and gypsum aggregates, as a function of additional water ( $w$ ) and mesoscale size ( $R_{meso}$ ). The phase boundary (marked as the white line in Fig. 3A) occurs at  $\Delta G_{tgy} = \Delta G_{agg}$  ( $\Delta G_{dif} = 0$ ), where the critical size of phase transformation decreases with more water addition (Supplementary Fig. 11). In such scenario, bassanite is favourable at the smaller  $w$  and  $R_{meso}$  (red and yellow coloured range in the lower left corner), while decreasing the added water content can correspondingly increase the opportunity to obtain the larger sized mesostructure of bassanite. In the absence of PVP ligands, the phase boundary of these two phases manifestly shifts to the corner with the even smaller water content and size, marked as the dotted line. It suggests that without ligands, bassanite phase can only exist at the nanoscale size, as confirmed by the statistical results in Fig. 3B. In contrast, the PVP ligands provide the chance to stabilize bassanite in solution with a relatively higher water ratio, thus facilitating the growth of bassanite into bulk size (Fig. 3B). The result suggests that the PVP ligands can effectively control the water availability by trapping water into hydrophilic groups of ligands (27), to change the conversion energy favorable for the growth of bassanite into bulk, instead of phase transforming into gypsum.

### **Mechanism of water-driven formation of bulk bassanite.**

To inquire the effect of ligands on the water-induced assembly and growth of bassanite at the molecular level, *ab initio* molecular dynamics (AIMD) were performed to simulate the behaviours of water molecules and n-vinyl-2-pyrrolidinone (NV2P) (the headgroup of PVP) on the (020) crystal plane, which is the typical lateral surface of bassanite nanorods for the assembly in the direction perpendicular to [102] (Fig. 2). The energy and temperature evolution

during the simulation process are shown in Supplementary Fig. 13, where the system is equilibrated after 2 ps.



**Fig. 4. AIMD analysis.** (A-C) Sequence of the sampled configurations observed along the AIMD trajectory using a NVE ensemble at 0, 1500, and 4800 fs. The trajectory refers to the simulation at the bassanite interface. (For water molecules, H: white; O in W1 and W2: red; For n-vinyl-2-pyrrolidinone (NV2P), C: cyan; N: blue. All the atoms in bassanite are represented as the grey solid spheres, except one Ca at the specific site close to W2 is marked in lime. (D, E) Evolution of the distance between the water molecules (W1 and W2) and the surface of bassanite or NV2P molecule as a function of time. The distance is recorded between O atom of water and Ca atom of bassanite ( $Ca_{Bassanite} - O_{W1}$  and  $Ca_{Bassanite} - O_{W2}$ ) or N atom in NV2P molecule ( $N_{NV2P} - O_{W1}$  and  $N_{NV2P} - O_{W2}$ ). The distance between Ca and N atoms ( $Ca_{Bassanite} - N_{NV2P}$ ) is presented as the reference to show the evolution of distance between bassanite surface and NV2P molecule.

Fig. 4 illustrates the details by recording the snapshots along a trajectory's segment, during which one of such events occurs (see Movie S1 in Supporting Information). It is seen that one of water molecules (W1), bind to NV2P at 1500 fs, and then drag the NV2P away from the bassanite surface (4800 fs) (Fig. 4A-C). In such way, the water available for bassanite transforming into gypsum can be effectively limited, and thus provide the chance for the growth

of metastable bassanite nanorods into bulk. On the other hand, when the water molecule moves the ligands together away from the particle surface, it can also produce a simple and effective attractive depletion force to trigger the hierarchical assembly of bassanite colloids into the mesostructure<sup>27,28</sup>. In the meantime, another water molecule (W2) is quickly trapped at the site with lower potential energy and then only relaxes near the specific site with defects (Fig. 4A-C).

Although the site comprises the atoms with unsaturated coordination to accommodate W2, the persistent chemical bond is still not formed (see the details in Fig. 4E). The trap of water molecules may give rise to the anisotropic growth of adsorbed water on the surface, which can increase the hydrophilicity of mineral surface and accelerates the assembly of particles in organic n-propanol solution<sup>29</sup>. As a result, both the desorption of surface-bonded PVP ligands and the formation of adsorbed water layers can facilitate the assembly of bassanite nanorods into mesostructure via particle attachment<sup>30</sup> (Supplementary Fig. 14).

The trajectory of water molecules is further quantified by recording the distance between O atom of water molecules and Ca atom of bassanite (highlighted in green in Fig. 4A-C), where W1 is initially located in the place with the same Ca-O and N-O distances as W2, but in a different direction. As shown in Fig. 4D, the distance between Ca and O in W1 increases rapidly from 10 Å to above 30 Å, and meanwhile, the distance between O in W1 and N in NV2P maintains 5-10 Å. Therefore, W1 is believed to move together with NV2P away from the surface of bassanite. While for W2 (Fig. 4E), O atom of W2 gradually approaches Ca atom of bassanite from 10 Å to 5 Å within 1 ps. However, the minimum distance is still much larger than the Ca-O bond (2.4 Å) in bassanite. This implies that O of W2 is not bonded to Ca in bassanite to transform into gypsum ( $\text{CaSO}_4 \cdot 2\text{H}_2\text{O}$ ), although they have maintained a closed distance due to the surface adsorption. In addition, the distance between O of W2 and N in NV2P quickly departs from less than 5 Å to 30 Å, indicating that W2 is free from NV2P. The simulation results demonstrate the presence of PVP on the bassanite can effectively trap water molecules in a proper pathway to direct bassanite growth via particle attachment, while keeping the structure not phase-transforming into gypsum.

In theory, even less than 0.385 wt% of excess water are enough to transform the metastable bassanite precursors into gypsum, when considering that 1.5 H<sub>2</sub>O molecules are needed for the

stoichiometric phase-transformation of  $\text{CaSO}_4 \cdot 0.5\text{H}_2\text{O}$  into  $\text{CaSO}_4 \cdot 2\text{H}_2\text{O}$ . It means that among the 3.85 wt% of water added to obtain bulk bassanite, most water molecules have not participated in the crystallization of the mineral hydrate to form gypsum. From the above AIMD simulation, it can be seen that when a certain amount of water is added to the bassanite nanorod precursor, some of these water molecules bind with PVP on the particle surface, while the other water molecules are trapped on the bassanite surface. The limitation of the water behaviours reduces the water availability for transformation of bassanite into gypsum, and thus facilitates the assembly of bassanite nanorods and subsequently the growth into bulk bassanite. We speculate that the water moves the ligands away from the assembly interface, providing a simple and effective attractive depletion forces to trigger the hierarchical assembly of bassanite colloids into the mesostructure<sup>27,28</sup>. However, Once the content of the added water exceeds the lowest water coverage on both PVP and bassanite nanoparticle surface, the remaining free-water molecules will trigger the energetically favourable phase transformation during the assembly of bassanite nanorods, leading to the final product of thermodynamically stable gypsum in solution.

## Discussion

In a nutshell, we have successfully decoupled the water-induced assembly and structural transformation favored by thermodynamics to obtain the bulk bassanite in solution at room temperature. Water activity, which can be mediated by PVP ligands, was proved to be critical in determining the phase structures of calcium sulfate during the hierarchical self-assembly process of bassanite nanorods. By controlling the added water amount in the system with PVP, the assembly of the nanorod precursors forms a hierarchical mesostructure and eventually evolves into bulk bassanite. The thermodynamic model was proposed to understand the crystallization and phase transformation of bulk bassanite and gypsum through non-classical particle assembly scenario. The AIMD simulations confirm that water molecules can be effectively trapped on the PVP-stabilized particle surface, facilitating the assembly and growth of bassanite nanorods into bulk. The results in this work not only shed light on the understanding of the role of (in)organic species mediated water activity for the formation of stable bulk bassanite in extreme environments on

Earth and Mars, but also allow for the facile and energy-saving fabrication of bulk bassanite materials for potential implications.

## **Materials and Methods**

### **Experimental details.**

All the reagents used in this study were purchased from Sino Pharm Chemical Reagent Co., Ltd., China. In a typical experiment, 1g polyvinyl pyrrolidone (PVP K30, average molecular weight is 52000) was added in 5 ml n-propanol (NPA) solution of  $\text{CaCl}_2$  (0.1 M), and the mixed solutions were continuously stirred at 350 r.p.m for 30 mins to obtain solution I. 26  $\mu\text{l}$   $\text{H}_2\text{SO}_4$  (containing 2 vol%  $\text{H}_2\text{O}$ ) was added to solution I and stir at 600 r.p.m for 10 mins to create yellow translucent colloidal solutions named solution II, where bassanite precursors are monodisperse. Afterwards, to systematically study the effect of the water content on the growth of this bassanite precursors, further experiments were carried out by adding 0-1.2 mL  $\text{H}_2\text{O}$  into solution II. This gave final water weight fractions ranging from 0 to 19.3 wt%. The solid samples were collected at selected time steps, washed with anhydrous methanol for 3 times, and vacuum-dried for characterization. All the above procedures were performed at room temperature ( $\sim 22^\circ\text{C}$ ).

### **Characterization.**

X-ray diffractometer (X' Pert3 Powder, PANalytical, Netherlands) is used to perform X-ray diffraction (XRD) measurement. Diffraction data were recorded with  $\text{Cu-K}\alpha$  radiation (40 kV, 40 mA) in the continuous scanning mode. The  $2\theta$  scan range was set from  $5^\circ$  to  $70^\circ$  in a step of  $0.026^\circ$  with a collection time of 51 s per step. SEM snapshot was performed with a Quattro C of Thermofisher scanning electron microscope equipped with an energy dispersive X-ray spectroscope.

For the High-resolution micro spectroscopic analyses, 20  $\mu\text{L}$  aliquots were rapidly directly onto holey carbon TEM grids in prior of three washes with anhydrous methanol (Agar Scientific), Then transferred it into a special anaerobic transfer holder. TEM images were collected by a JEOL JEM-2010 TEM operated at 200 kV.

As for FTIR, aliquots collected at selected time steps were rapidly vacuum filtered and washed three times with anhydrous methanol, then the residues were vacuum-dried for 2 h before spread them on an attenuated total reflectance (ATR) unit mounted on a Perkin-Elmer FTIR Spectrum 100 instrument. Data were collected in reflection mode at a resolution of  $1\text{ cm}^{-1}$ , and were averaged over a total of 8 scans.

### Calculation details.

All the surface energy calculations were implemented by applying the projector-augmented wave (PAW)<sup>31,32</sup> approach VASPsol<sup>33</sup> solvation and executed in the Vienna *ab initio* simulation package (VASP)<sup>34,35</sup>. Electronic exchange and correlation energy were handled by employing the spin-polarized generalized gradient approximation (GGA) of Perdew-Burke-Ernzerhof (PBE)<sup>36</sup>. We used a monoclinic cell for bassanite and the cut-off energy is set at 600 eV for the plane-wave basis restriction in all the calculations. Gamma-centered k-point meshes of  $(50/a) \cdot (50/b) \cdot (50/c)$  and  $(50/a) \cdot (50/b) \cdot 1$  was used for slab calculations, respectively, with non-integer values rounded up to the nearest integer. In all the calculations, the forces acting on all the atoms are less than  $0.03\text{ eV}/\text{\AA}$  in the fully relaxed structures, and self-consistency accuracy of  $10^{-6}\text{ eV}$  is reached for electronic loops. The surface slab with the vacuum layer in  $20\text{ \AA}$  was generated from the optimized bulk in terms of the interaction of periodic influence. For the calculation of specific surface energy, the Wulff shape reconstruction was used to justify the variation of exposed bassanite surface<sup>37</sup>.

We performed all *ab initio* molecular dynamics by employing the CP2K<sup>38</sup> program package. All the atoms were described by the DZVP-MOLOPTRS-GTH basis sets<sup>39</sup>. In the mixed Gaussian-plane-wave scheme (GPW), the atomic core electrons are described by Goedecker–Teter–Hutter pseudopotentials<sup>40</sup>. The Perdew-Burke-Ernzerhof (PBE) functional with D3<sup>41</sup> correction was adopted for describing the electronic structure<sup>42,43</sup>, and a cutoff of 800 Ry for the auxiliary plane-wave basis set was used.

AIMD simulations on the bassanite surface were performed with simulation cells of 160 atoms. Production runs of 5 ps and the gamma-only k-mesh were used in all AIMD calculations and analysis. The cell of bassanite<sup>44</sup> containing 131 atoms was used to simulate a surface/bulk

crystal. Four water molecules are placed on the (020) surface near a NV2P molecule. The NV2P is initially placed closed to the surface of bassanite, while the minimum distance between water molecules and bassanite surface is set to be larger than 4 Å to avoid high initial kinetic energy. The successive simulations with NVE ensemble were carried out with a time step of 1 fs, where the initial temperature was set at 300 K by a Nose-Hoover chain thermostat<sup>45</sup>.

## Data availability

All data are available from the authors upon reasonable request.

## Code availability

All Python and Mathematica scripts used for the theoretical modelling are available from the authors upon reasonable request.

## References

1. Freyer D, Voigt W. Crystallization and phase stability of CaSO<sub>4</sub> and CaSO<sub>4</sub>-based salts. *Monatsh. Chem.* **134**, 693-719 (2003).
2. Buick R, Dunlop JSR. Evaporitic sediments of Early Archaean age from the Warrawoona Group, North Pole, Western Australia. *Sedimentology* **37**, 247-277 (1990).
3. Van Driessche AES, Benning LG, Rodriguez-Blanco JD, Ossorio M, Bots P, Garcia-Ruiz JM. The Role and Implications of Bassanite as a Stable Precursor Phase to Gypsum Precipitation. *Science* **336**, 69-72 (2012).
4. Mees F, Tursina TV. Chapter 11 - Salt Minerals in Saline Soils and Salt Crusts. In: *Interpretation of Micromorphological Features of Soils and Regoliths (Second Edition)* (eds Stoops G, Marcelino V, Mees F). Elsevier (2018).
5. Ehlmann BL, *et al.* Subsurface water and clay mineral formation during the early history of Mars. *Nature* **479**, 53-60 (2011).
6. Bibring J-P, *et al.* Global Mineralogical and Aqueous Mars History Derived from OMEGA/Mars Express Data. *Science* **312**, 400-404 (2006).
7. Weiss H, Bräu MF. How Much Water Does Calcined Gypsum Contain? *Angew. Chem. Int. Ed.* **48**, 3520-3524 (2009).

8. Stawski TM, van Driessche AES, Ossorio M, Rodriguez-Blanco JD, Besselink R, Benning LG. Formation of calcium sulfate through the aggregation of sub-3 nanometre primary species. *Nat. Commun.* **7**, (2016).
9. Tiemann H, Sötje I, Jarms G, Paulmann C, Epple M, Hasse B. Calcium sulfate hemihydrate in statoliths of deep-sea medusae. *Dalton Trans.*, 1266-1268 (2002).
10. Becker A, *et al.* Calcium sulfate hemihydrate is the inorganic mineral in statoliths of Scyphozoan medusae (Cnidaria). *Dalton Trans.*, 1545-1550 (2005).
11. Weiner S, Pinkas I, Kossoy A, Feldman Y. Calcium Sulfate Hemihydrate (Bassanite) Crystals in the Wood of the Tamarix Tree. *Minerals* **11**, (2021).
12. Banfield JF, Welch SA, Zhang HZ, Ebert TT, Penn RL. Aggregation-based crystal growth and microstructure development in natural iron oxyhydroxide biomineralization products. *Science* **289**, 751-754 (2000).
13. Colfen H, Mann S. Higher-order organization by mesoscale self-assembly and transformation of hybrid nanostructures. *Angew. Chem. Int. Ed.* **42**, 2350-2365 (2003).
14. De Yoreo JJ, *et al.* Crystallization by particle attachment in synthetic, biogenic, and geologic environments. *Science* **349**, 6760 (2015).
15. Morgado G, Masurel L, Rhodes Z, Lespiat R, Retot H, Lemarchand A. Kinetics of plaster hydration and structure of gypsum: Experiments and kinetic Monte Carlo simulations with added gypsum seeds. *J. Cryst. Growth* **507**, 124-133 (2019).
16. Tritschler U, Van Driessche AES, Kempter A, Kellermeier M, Colfen H. Controlling the Selective Formation of Calcium Sulfate Polymorphs at Room Temperature. *Angew. Chem. Int. Ed.* **54**, 4083-4086 (2015).
17. Tosca NJ, Knoll AH, McLennan SM. Water Activity and the Challenge for Life on Early Mars. *Science* **320**, 1204 (2008).
18. Lenders JJM, *et al.* High-Magnesian Calcite Mesocrystals: A Coordination Chemistry Approach. *J. Am. Chem. Soc.* **134**, 1367-1373 (2012).
19. Falini G, Gazzano M, Ripamonti A. Calcite crystallization on gelatin films containing polyelectrolytes. *Adv. Mater.* **6**, 46-48 (1994).
20. Zhang J, *et al.* A multistep oriented attachment kinetics: Coarsening of ZnS nanoparticle in concentrated NaOH. *J. Am. Chem. Soc.* **128**, 12981-12987 (2006).
21. Wu K, Ma CY, Liu JJ, Zhang Y, Wang X, Design. Measurement of crystal face specific growth kinetics. *Cryst. Growth Des.* **16**, 4855-4868 (2016).
22. Wang H-W, *et al.* Structure and Stability of SnO<sub>2</sub> Nanocrystals and Surface-Bound Water Species. *J. Am. Chem. Soc.* **135**, 6885-6895 (2013).
23. Raju M, van Duin ACT, Fichthorn KA. Mechanisms of Oriented Attachment of TiO<sub>2</sub> Nanocrystals in Vacuum and Humid Environments: Reactive Molecular Dynamics. *Nano Lett.* **14**, 1836-1842 (2014).
24. Tran R, *et al.* Surface energies of elemental crystals. *Sci. Data* **3**, 160080-160080 (2016).
25. Atkins P, Overton T. *Shriver and Atkins' inorganic chemistry*. Oxford University Press, USA (2010).
26. Mirabello G, *et al.* Crystallization by particle attachment is a colloidal assembly process. *Nat. Mater.* **19**, 391-396 (2020).

27. Asakura S, Oosawa F. On interaction between two bodies immersed in a solution of macromolecules. *J. Chem. Phys.* **22**, 1255-1256 (1954).
28. Zhang J, Lang PR, Meyer M, Dhont JKG. Synthesis and Self-Assembly of Squarelike PbCrO<sub>4</sub> Nanoplatelets via Micelle-Mediated Depletion Attraction. *Langmuir* **29**, 4679-4687 (2013).
29. Yalcin SE, Legg BA, Yeşilbaş M, Malvankar NS, Boily J-F. Direct observation of anisotropic growth of water films on minerals driven by defects and surface tension. *Science Advances* **6**, 9708 (2020).
30. Stawski TM, van Driessche AES, Ossorio M, Diego Rodriguez-Blanco J, Besselink R, Benning LG. Formation of calcium sulfate through the aggregation of sub-3 nanometre primary species. *Nat. Commun.* **7**, 11177 (2016).
31. Blöchl PE. Projector augmented-wave method. *Phys. Rev. B* **50**, 17953 (1994).
32. Kresse G, Joubert D. From ultrasoft pseudopotentials to the projector augmented-wave method. *Phys. Rev. B* **59**, 1758 (1999).
33. Mathew K, Sundararaman R, Letchworth-Weaver K, Arias TA, Hennig RG. Implicit solvation model for density-functional study of nanocrystal surfaces and reaction pathways. *J. Chem. Phys.* **140**, 084106 (2014).
34. Kresse G, Furthmüller J. Efficiency of ab-initio total energy calculations for metals and semiconductors using a plane-wave basis set. *Comput. Mater. Sci.* **6**, 15-50 (1996).
35. Kresse G, Furthmüller J. Efficient iterative schemes for ab initio total-energy calculations using a plane-wave basis set. *Phys. Rev. B* **54**, 11169 (1996).
36. Perdew JP, Burke K, Ernzerhof M. Generalized gradient approximation made simple. *Phys. Rev. Lett.* **77**, 3865 (1996).
37. Wang Q, Manzano H, Guo Y, Lopez-Arbeloa I, Shen X. Hydration mechanism of reactive and passive dicalcium silicate polymorphs from molecular simulations. *J. Phys. Chem.* **119**, 19869-19875 (2015).
38. Hutter J, Iannuzzi M, Schiffmann F, VandeVondele J. cp2k: atomistic simulations of condensed matter systems. *Rev. Comput. Mol. Sci.* **4**, 15-25 (2014).
39. VandeVondele J, Hutter J. Gaussian basis sets for accurate calculations on molecular systems in gas and condensed phases. *J. Chem. Phys.* **127**, 114105 (2007).
40. Goedecker S, Teter M, Hutter J. Separable dual-space Gaussian pseudopotentials. *J. Chem. Phys.* **54**, 1703 (1996).
41. Grimme S, Antony J, Ehrlich S, Krieg H. A consistent and accurate ab initio parametrization of density functional dispersion correction (DFT-D) for the 94 elements H-Pu. *J. Chem. Phys.* **132**, 154104 (2010).
42. Becke AD. Density-functional exchange-energy approximation with correct asymptotic behavior. *Phys. Rev. A* **38**, 3098 (1988).
43. Lee C, Yang W, Parr RG. Development of the Colle-Salvetti correlation-energy formula into a functional of the electron density. *Phys. Rev. B* **37**, 785 (1988).
44. Powell DA. The  $\alpha$ - and  $\beta$ -forms of calcium sulphate hemihydrate. *Nature* **185**, 375-376 (1960).
45. Nosé S. A molecular dynamics method for simulations in the canonical ensemble. *Mol. Phys.* **52**, 255-268 (1984).

## **Acknowledgments**

The authors acknowledge the financial support from the National Key Research and Development Program of China (2017YFA0207204 and 2016YFA0203101), the National Natural Science Foundation of China (21836002, 21876190 and 21902182), the Fundamental Research Funds for the Central Universities (2020001840 and 2019QH01).

## **Competing interests**

The authors declare no competing interests.

## **Additional information**

Supplementary information is available for this paper.

## Supplementary Files

This is a list of supplementary files associated with this preprint. Click to download.

- [SupplementaryMaterialstext.docx](#)
- [SupportingVideo.mp4](#)